

# Incorporation of Dynamic Strain Aging Into a Viscoplastic Self-Consistent Model for Predicting the Negative Strain Rate Sensitivity of Hadfield Steel

B. Bal

Advanced Materials Group (AMG),  
Department of Mechanical Engineering,  
Koç University,  
Sariyer, İstanbul 34450, Turkey

B. Gümüş

Advanced Materials Group (AMG),  
Department of Mechanical Engineering,  
Koç University,  
Sariyer, İstanbul 34450, Turkey

D. Canadinc<sup>1</sup>

Advanced Materials Group (AMG),  
Department of Mechanical Engineering,  
Koç University,  
Sariyer,  
İstanbul 34450, Turkey  
e-mail: dcanadinc@ku.edu.tr

A new multiscale modeling approach is proposed to predict the contributions of dynamic strain aging (DSA) and the resulting negative strain rate sensitivity (NSRS) on the unusual strain-hardening response of Hadfield steel (HS). Mechanical response of HS was obtained from monotonic and strain rate jump experiments under uniaxial tensile loading within the  $10^{-4}$  to  $10^{-1} \text{ s}^{-1}$  strain rate range. Specifically, a unique strain-hardening model was proposed that incorporates the atomic-level local instabilities imposed upon by the pinning of dislocations by diffusing carbon atoms to the classical Voce hardening. The novelty of the current approach is the computation of the shear stress contribution imposed on arrested dislocations leading to DSA at the atomic level, which is then implemented to the overall strain-hardening rule at the microscopic level. The new model not only successfully predicts the role of DSA and the resulting NSRS on the macroscopic deformation response of HS but also opens the venue for accurately predicting the deformation response of rate-sensitive metallic materials under any given loading condition. [DOI: 10.1115/1.4033072]

**Keywords:** crystal plasticity, negative strain rate sensitivity, dynamic strain aging, polycrystal, high-manganese austenitic steel

## 1 Introduction

Despite having been subject to several investigations and a topic of debate for decades, the unusual strain-hardening response of HS has not been linked to a clear cause yet. This superior steel, which exhibits high wear resistance combined with significant ductility and strength, possesses an inherent toughness and an exceptional work-hardening capability [1–12]. The lattice structure is face-centered cubic (FCC) at room temperature, mainly due to chemical stabilization of austenite by carbon (C) and manganese (Mn) in the microstructure [11], resulting in improved strain-hardening behavior. Previously, the unusually high strain-hardening capacity of HS was often attributed to the formation of twin boundaries that provided strong barriers against dislocation motion [2,4,13–16]. In addition to twin boundaries, interruption of the glide dislocation path by stacking faults [3,17] has also been forwarded as the reason for the aforementioned unusual strain hardening exhibited by HS. It was also shown that alloying of HS with aluminum (HSwAl) further increased the strain-hardening rate by enhancing the formation of high-density dislocation walls (HDDWs) and their interactions with active slip systems, as demonstrated by thorough transmission electron microscopy investigations [5,18]. A viscoplastic self-consistent (VPSC) model was proposed [5], which takes into account the interaction of HDDWs with the glide dislocations, leading to the increased strain hardening observed in single crystals of HSwAl, which then was extended to polycrystals of HSwAl [18]. The study has shown that

the model is also applicable to simulate the deformation response of polycrystalline HSwAl [18].

In addition to the aforementioned arguments, DSA was also forwarded the reason underlying the rapid strain hardening of HS [1,12]. In particular, based on experimental observations on HS within a wide range of temperatures promoting different levels, the competing slip and twin activities, DSA, brought about by the reorientation of carbon members of Mn-C couples in the cores of dislocations, were argued to be the primary cause of rapid strain hardening in HS [1]. This argument was supported by a model that accounts for the change in the probability of possible metal–interstitial atom pairs during plastic deformation of HS, where enhanced C diffusion is facilitated by increased dislocation density [12]. Specifically, the passage of a dislocation destroys the local order, and the slip-induced chemical energy change also affects the number and distribution of nearest neighbor chemical bonds, such that the distribution of metal–interstitial atom pairs also varies throughout the deformation [12]. Even though this model well demonstrated the contribution of DSA to the overall hardening [12], the results were limited to reflecting the deformation-induced statistical changes in the distribution of metal–interstitial atom pairs and the corresponding chemical energy changes.

Recently, an experimental study combining the digital image correlation (DIC) with strain rate jump tests within a strain rate range of  $10^{-4}$  to  $10^{-1} \text{ s}^{-1}$  [19] revealed that DSA indeed plays a critical role on the work-hardening response of HS. Specifically, it was demonstrated that HS exhibits NSRS within the aforementioned strain rate range, such that increasing strain rate may cause softening of the material, warranting further investigation of the contribution of DSA to the overall hardening response of HS. Considering the fact that various types of applications employing

<sup>1</sup>Corresponding author.

Contributed by the Materials Division of ASME for publication in the JOURNAL OF ENGINEERING MATERIALS AND TECHNOLOGY. Manuscript received November 17, 2015; final manuscript received March 4, 2016; published online May 10, 2016. Assoc. Editor: Antonios Kontos.

HS, such as in mining or railroad industries, involve continuous wear and deformation of the material, properly addressing this problem is very important to ensure a predictable response of the corresponding parts made of HS. With this motivation, the current work focuses on the incorporation of DSA into a crystal plasticity model to predict both the role of DSA on the strain-hardening behavior of HS and the previously observed NSRS exhibited by this material. The outcome of this effort is expected to open a venue for a better prediction of the deformation response of HS even in the presence of NSRS.

Despite the very limited number of studies focusing on DSA in HS, DSA and rate sensitivity in metallic alloys have been the subject of interest in several works, which have laid out the fundamentals and important details of DSA [20–27]. Consequently, theoretical framework of DSA was established in detail, and numerical models were proposed to predict DSA. Nevertheless, the focus of the numerical simulations was confined mostly to the statistical analysis of shear localization during deformation and the Portevin Le Chatelier (PLC) effect. Some works included numerical simulations of stress-strain response; however, neither these works nor others to follow have so far presented a thorough analysis targeting the effects of rate sensitivity on the macroscopic deformation response and its prediction.

The PLC effect brought about by the instability of dislocation motion due to solute atoms in the lattice is commonly associated with DSA and was investigated experimentally to some extent for metallic materials. However, the atomic- and micro-scale basis of the phenomenon makes monitoring of the PLC activities difficult with conventional testing methods. Thus, many of the corresponding experimental studies employed advanced techniques, such as acoustic emission [28], DIC [29], and laser scanning extensometry [30]. However, difficulty in distinguishing the PLC effect and the signals arising from acoustic emission source, dependence of the DIC results' reliability on the sample surface preparation and imaging quality, and possibility of obtaining only one-dimensional information in laser scanning extensometry [31] make these techniques impractical. This, on the other hand, makes modeling a practical and attractive means of studying the contribution of DSA, and hence the PLC effect, to the overall work-hardening behavior of metallic materials.

The current study was undertaken with the intention of clarifying the role of DSA on the strain-hardening response of HS through modeling. For this purpose, a crystal plasticity model was developed incorporating DSA into standard VPSC model, where the classical Voce type hardening was modified by taking into account the flow stress contribution that reflects the stress field imposed on the arrested dislocations due to rate-dependent solute field surrounding them. The results then were compared to the experimental results obtained from strain rate jump tests on HS polycrystals. The novelty of the modeling effort presented herein lies in the implementation of the contribution of the DSA to the overall hardening response of the material, which required the proper treatment of an atomic-scale problem at the microscale. The simulation results demonstrated the success of the proposed model in predicting the role of DSA on the mechanical response of the HS, including the NSRS exhibited by this material. Overall, the new model proposed in this paper opens a venue for proper treatment of DSA and predicting the NSRS in rate-sensitive metallic materials.

## 2 Materials and Methods

The material investigated in this study is HS with a chemical composition of 12.44 wt.% Mn, 1.10 wt.% C, and balance Fe and a FCC structure. The samples were extracted from railroad frogs taken from service. Electrodischarge machining was utilized to cut small-scale dog-bone shaped tension specimens. The samples were tested utilizing a servohydraulic test frame equipped with a digital controller. A miniature extensometer with a gauge length of 3 mm was employed for accurate strain measurement in the

gauge section. Two types of experiments were carried out under tensile loading: Monotonic stress-strain experiments and strain rate jump tests. The experiments were conducted at strain rates within the range of  $10^{-4}$  to  $10^{-1}$  s $^{-1}$ . The samples were analyzed with X-ray diffraction prior to experiments in order to determine the initial textures in the loading direction, and the initial samples possessed a random texture [18].

At room temperature, HS exhibited NSRS in the strain rate range of  $10^{-4}$  to  $10^{-1}$  s $^{-1}$  as shown in Fig. 1. Moreover, stress drops due to flow localization follow a periodic pattern, typical of PLC effect [19]. Figure 2 presents the results of strain rate jump test, further demonstrating the NSRS of HS. An abrupt change in the strain rate results in an instantaneous change in flow stress,  $\Delta\sigma_i$ , which is always positive [25], and this change in the deformation response is reflected by the instantaneous strain rate sensitivity, denoted by,  $M_i = d\sigma_i/d\ln\dot{\epsilon}$ . However, whether the strain rate sensitivity is negative or positive is based on the steady-state strain rate sensitivity,  $M_s = d\sigma_{ss}/d\ln\dot{\epsilon}$ , which considers the difference in stable flow stress,  $\Delta\sigma_{ss}$ , following the strain rate jump [25,26]. In the NSRS regime,  $\Delta\sigma_{ss}$  and  $M_s$  are negative and become positive outside the NSRS regime (Fig. 2).

## 3 Theory and Calculations

### 3.1 Modeling the Role of DSA on Strain Hardening.

In order to better understand the influence of DSA on the deformation response of HS, the DSA was incorporated into standard VPSC model as an additional mechanism affecting the strain hardening. The classical Voce-hardening scheme was modified to accomplish this, such that the role of DSA was expressed in terms of shear stress field imposed on arrested dislocations due to surrounding carbon atom field. The details of this unique formulation are presented in this section.

The DSA as a phenomenon is attributed to the pinning of mobile dislocations arrested at obstacles, by solute atoms diffusing in the matrix [32]. Upon hindering of dislocation glide by obstacles, there is an elapse of time before the dislocations overcome the obstacles. The average time the dislocations stay arrested at obstacles throughout the matrix is defined as the waiting time,  $t_w$ , and is proportional to the density of mobile dislocations ( $\rho_m$ ), the Burgers vector magnitude ( $b$ ), the dislocation mean free path ( $L$ ), and the inverse of strain rate ( $1/\dot{\epsilon}$ ). Hence, the Orowan equation defines the waiting time as  $t_w = \rho_m b L / \dot{\epsilon}$  [25,26,32]. During the waiting time, solute atoms might diffuse into the arrested dislocations, leading to DSA [32]. Overall, DSA depends on temperature, time of arrest of dislocations at the obstacles ( $t_w$ ), strain rate, solute concentration, and diffusion coefficient. As the waiting time is directly related to strain rate, consequently, DSA is expected to influence the dependence of stress on the strain rate. Previously, the influence of the DSA on the flow stress was taken into account through an Arrhenius-based constitutive relationship [25,26]. In this study, we consider the contribution of DSA to the critical

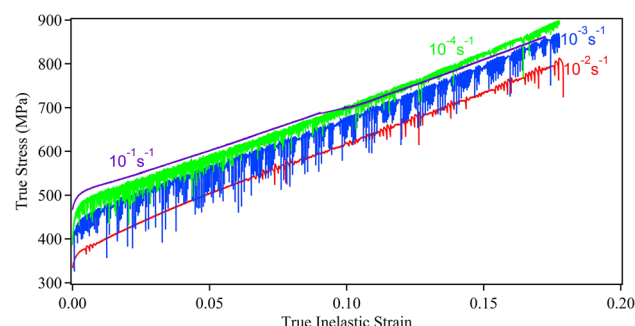


**Fig. 1** The room temperature uniaxial tensile deformation response of HS obtained at different strain rates. The data were recompiled from Ref. [19].

resolved shear stress in each grain (or single crystal). The contribution due to DSA was taken into account through the additional shear stress on the arrested dislocations due to the diffusing solute atoms pinning them [33]. The role of carbon solute field around arrested dislocations is considered under conditions where carbon is in equilibrium with local stresses [33]. All the mobile dislocations that are pinned by the diffusing solute carbon atoms are considered to be the positive-edge dislocations for the sake of simplicity. In the current study, the shear stress imposed on a positive-edge dislocation due to carbon atom is modeled by a continuous distribution of dilatation lines whose strength depends on the local carbon concentration around arrested edge dislocations.

With respect to solute concentration, the velocity of solute atoms relative to positive-edge dislocations that move in the direction of the unit vector  $\underline{i}$  is considered to consist of three components [21]: The drift velocity  $v_1 = -D\underline{\nabla}W^{\text{int}}/kT$  due to the field of force  $-\underline{\nabla}W^{\text{int}}$ , diffusion velocity  $v_2 = -D\underline{\nabla}C/C$  due to concentration gradients, and a constant velocity  $v_i$  due to dislocation motion. The field of force  $-\underline{\nabla}W^{\text{int}}$  is simply the negative gradient of the interaction energy,  $W^{\text{int}}$ , and  $C$ ,  $D$ ,  $k$ , and  $T$  represent the solute atom distribution, diffusion coefficient, Boltzmann's constant, and the absolute temperature, which was taken as 298 K in the current work, respectively. As a result, the velocity of solute atoms relative to dislocations is given by [21]

$$\underline{v} = \underline{v}_1 + \underline{v}_2 + \underline{v}_i = -\frac{D\underline{\nabla}W^{\text{int}}}{kT} - \frac{D\underline{\nabla}C}{C} + \underline{v}_i \quad (1)$$

The interaction energy ( $W^{\text{int}}$ ) between a positive-edge dislocation and an atom in substitutional solution is defined as [20]

$$W^{\text{int}}(r, \alpha) = \frac{4}{3} \mu \chi r_a^3 b \frac{1+v \sin \alpha}{1-v} \quad (2)$$

The terms  $r$  and  $\alpha$  define the cylindrical coordinate system with the positive-edge dislocation at the origin (Fig. 3). The atomic radii of the solvent and solute atoms are given by  $r_a$  and  $r_a(1+\chi) = r_c$ , respectively. Poisson's ratio and modulus of rigidity are represented by  $V$  and  $\mu$ , respectively.

Assuming steady-state of motion, the continuity condition requires that  $\underline{\nabla}(C\underline{v}) = 0$ , which eventually yields the solute atom concentration function as [21]

$$C(r, \alpha) = C_0 \exp \left\{ -\frac{W^{\text{int}}(r, \alpha)}{kT} \right\} \quad (3)$$

where  $C_0$  is the average solute concentration of the alloy. In order to calculate the shear stress imposed on a positive-edge dislocation due to solute carbon atom, the solute atom concentration calculation is needed. Equations (1)–(3) were used to model the solute atom concentration distribution with respect to polar coordinates at the steady-state condition, which requires  $\underline{\nabla}(C\underline{v}) = 0$ .

In this basic form of Eq. (3), however, the solute atom concentration distribution remains valid for steady-state equilibrium and

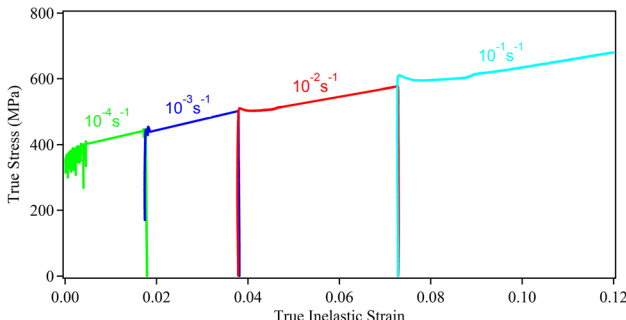


Fig. 2 Results of a representative strain rate jump test. The data were recompiled from Ref. [19].

does not reflect the time dependency, which is crucial for DSA. This time dependency of the solute atom concentration was well established in previous works [25,26]. Accordingly, the solute atom concentration is expressed as

$$C(r, \alpha) = C_0 \exp \left\{ (K(r, \alpha)Dt_a)^{\frac{2}{3}} \right\} \quad (4)$$

In Eq. (4), the term  $K(r, \alpha)D$  is the inverse of characteristic solute diffusion time,  $t_d$ , such that  $t_d = (K(r, \alpha)D)^{-1}$  [26]. Thereby, both the time dependency of the solute atom concentration and the competing velocities of diffusion and dislocation motion are taken into account in the definition of the solute atom concentration,  $C(r, \alpha)$ . Thus, for nonsteady-state condition, the solute atom concentration was modeled using Eq. (4). The term  $K(r, \alpha)$  includes the solute-dislocation binding energy, and  $t_a$  represents the aging time, which is the effective time period for which the dislocations are aged. It was shown that the effective aging time of the dislocations ( $t_a$ ) by the solute atoms pinning them is less than the waiting time,  $t_w$ , and therefore is used to establish the time dependency of the solute atom concentration [25]. The aging time is related to the waiting time as [25,34,35]

$$\frac{dt_a}{dt} = 1 - \frac{t_a}{t_w} \quad (5)$$

Considering the definition of the waiting time given by the Orowan equation, the aging time  $t_a$  is a function of strain and strain rate history. Thus, the time dependency of  $t_a$  determines the transient behavior of the solute concentration,  $C(r, \alpha)$ . From Eq. (5), it also follows that the aging time will be equal to the waiting time, i.e.,  $t_a = t_w$ , only for steady-state conditions [25]. For nonsteady state case, the time-dependent average waiting time is a function of fundamental attempt frequency,  $v_0$ , and energy barrier,  $E$ , which depends on the effective resolved shear stress,  $\tau_{\text{eff}}$ , acting on current time  $t$  [36–38]. The attempt frequency depends on mobile dislocation density, burgers vector, and the Debye frequency,  $v_D$ , which is a function of both density of the lattice and the speed of sound [39]. Specifically, the average waiting time can be expressed as

$$t_w = e^{\Delta E(\tau_{\text{eff}}^*)/kT} / v_0 \quad (6)$$

In the presence of solute atoms in the host matrix, a much higher energy barrier must be overcome by an edge dislocation to glide, which induces localized plasticity. Therefore, modeling energy barrier is crucial for our model. Several energy barrier models were proposed associated with different kinds of obstacles [26,40–42]. For short-range obstacles, which are more sensitive to

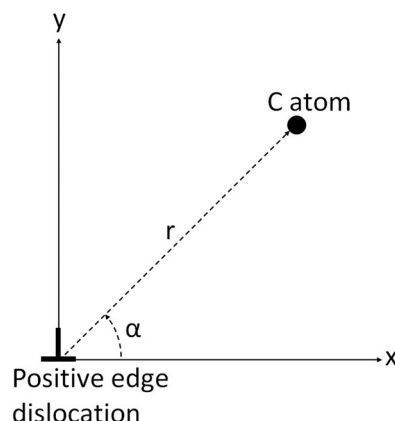


Fig. 3 Cylindrical coordinate system utilized to describe the location of an interstitial C atom with respect to a positive-edge dislocation

thermal activation, a useful phenomenological generalization of stress-dependent energy barrier model was suggested:

$$E(\tau_{\text{eff}}^{\alpha}) = E_0 \left[ 1 - \left( \frac{\tau_{\text{eff}}^{\alpha}}{s_0} \right)^p \right]^q \quad (7)$$

where  $E_0$  is the zero effective shear stress activation energy,  $p$  and  $q$  are the profiling parameters, and constant  $s_0$  is thermal slip resistance at 0 K, i.e., Peierls stress [39]. Initial effective shear stress activation energy and Peierls stress values were taken for an host iron matrix [39], assuming that an iron matrix represents the HS matrix, since it is extremely difficult to model the actual HS matrix owing to the large number of constituent elements [33]. Taking profiling parameters  $p$  and  $q$ , 1/2 and 3/2, respectively, is adequately accurate for all the systems [43].

In order to model the energy barrier, the effective shear stress needs to be calculated. The effective resolved shear stress on slip system  $\alpha$  can be formulated as the difference between resolved external stress,  $\tau$ , and summation of resolved back stress representing the slip system resistance,  $s_{\alpha}$ , and constant thermal stress,  $\tau_a$  [38,39,44,45]. Therefore, Eq. (8) was used to calculate effective shear stress, which was then used to model the energy barrier

$$\tau_{\text{eff}}^{\alpha} = |\tau^{\alpha}| - s_{\alpha}^{\alpha} - \tau_a^{\alpha} \quad (8)$$

The proposed crystal plasticity model can be decomposed into plastic deformation gradient due to primary slip, and elastic deformation gradient including lattice stretching and rotation. Constitutive law for elastic materials includes the second Piola-Kirchhoff stress tensor,  $T^*$ , and the right Cauchy-Green strain tensor,  $C^* = F^{*T}F^*$ , whereas in isotropic elastic materials Cauchy stress tensor is a function of the left Cauchy-Green strain tensor,  $B^* = F^*F^{*T}$ . Since elastic stretch can be neglected in metallic materials,  $\tau^{\alpha}$  can be expressed as [39,46–48]

$$\tau^{\alpha} = (C^*T^*) : s_0^{\alpha} \cong T^* : s_0^{\alpha} \quad (9)$$

The resolved back stress comes into picture because of both short-term and long-term dislocation interactions during dislocation motion on the slip systems and it can be expressed using Taylor hardening model as [39,45,49]

$$s_{\alpha}^{\alpha} = \mu b \sqrt{\sum_{\alpha=1}^N q_p A^{\alpha} \rho_{\text{total}}^{\alpha}} \quad (10)$$

where  $q_p$  is the dislocation barrier strength,  $A^{\alpha}$  is the slip system dislocation interaction coefficients matrix, and  $\rho_{\text{total}}^{\alpha}$  is the slip system dislocation density which is the summation of mobile and immobile dislocations. In our model, the dislocation density is considered in a Taylor format [45,49], and thus, it was solved in an implicit manner and a specific value was not assigned. Furthermore, the storage of statistically stored dislocations (SSDs) is a result of random trapping of mobile dislocations, and all the geometrically necessary dislocations (GNDs) are assumed to be immobile. Moreover, the screw GND densities were ignored and only edge SSD and GND densities (with the total number of slip systems  $N = 12$ ) were considered based on the balance between accumulation and annihilation rates [45,50,51]. Therefore, latent hardening caused by dislocation gradient on a primary slip system was calculated through Eq. (10).

Accordingly, the shear stress,  $\tau_{CD}$ , imposed on a positive-edge dislocation due to the surrounding solute atom concentration is given by [33,52]

$$\tau_{CD} = -\frac{\mu}{2\pi(1-v)N_A} \int_0^{2\pi} \int_{r_i}^{r_o} C(r, a) \frac{\sin 2\alpha}{r} dr d\alpha \quad (11)$$

In Eq. (11), the terms  $V_C$  and  $N_A$  represent the partial molar volume of carbon and the Avogadro's number ( $6.024 \times 10^{23}$

molecules/mole). The inner and outer cutoff radii of the carbon atmosphere surrounding the edge dislocation are given by  $r_i$  and  $r_o$ , respectively. It should be noted that the interaction energy given by Eq. (2) is not valid at  $r_i = 0$ , because the elastic continuum theory is not applicable at the origin (Fig. 3). Based on previous work,  $r_i = b$  and  $r_o = 10 \cdot b$  are assigned as the integration limits for Eq. (11).

The shear stress given by Eq. (11) represents the additional shear stress on a single edge dislocation due to the surrounding solute (carbon) atom concentration. To be able to account for the solute effect on the flow stress, we consider the quantity given by Eq. (11) to represent an average value throughout each grain, implying that the hardening formulation needs to be modified to include this average contribution in order to account for DSA influence on the overall hardening response. The constants utilized in the current DSA model are presented in Table 1.

**3.2 Modeling of Slip-Dominant Deformation Behavior in the Presence of DSA.** The modified VPSC algorithm utilized in this study accounts for the deformation in the plastic zone only and considers the plastic deformation to take place when one or more slip or twinning systems become active. The classical Voce-hardening scheme [53] is utilized to define the work hardening of the material, such that the microscopic flow stress is updated for each increment according to the following equation:

$$\dot{\tau} = \sum_n \left\{ \theta_0 \left( \frac{\tau_s - \tau}{\tau_s - \tau_0} \right) \right\} \left| \dot{\gamma}^n \right| \quad (12)$$

where  $\theta_0$  is the constant strain-hardening rate, and  $\tau_0$  is the reference strength, which is usually taken as the initial microscopic yield strength calculated based on the experimental macroscopic yield strength [5]. The term  $\tau_s$  represents the saturation stress in the absence of geometric effects, or the threshold stress, while the shear strain rate of the  $n$ th active system is represented by  $\dot{\gamma}^n$ . The hardening can be defined by an extended Voce law [5], which is characterized by the evolution of the threshold stress ( $\tau^s$ ) with accumulated shear strain ( $\Gamma$ ) in each grain

$$\tau^s = \tau_0 + (\tau_1 + \theta_1 \Gamma) \left( 1 - \exp \left( -\frac{\theta_0 \Gamma}{\tau_1} \right) \right) \quad (13)$$

where  $\tau_0$  is the reference strength, and  $\tau_1$ ,  $\theta_0$ , and  $\theta_1$  are the parameters that define the hardening behavior. The hardening law defined by Eq. (13) characterizes the onset of plasticity and the saturation of threshold stress at larger strains.

When modified to account for the contribution of DSA, the classical Voce-hardening scheme becomes

$$\dot{\tau} = \sum_n \left\{ \theta_0 \left( \frac{\tau_s - \tau}{\tau_s - \tau_0} \right) \right\} \left| \dot{\gamma}^n \right| + M_i S \frac{d\tau_{CD}}{dt} \quad (14)$$

where  $M_i$  is the instantaneous strain rate sensitivity that takes into account the abrupt strain rate changes during deformation, and  $S$  is the scaling factor that reflects the contribution to hardening throughout the whole grain and it was used as a fitting parameter to reflect the cumulative effects of atomistic level DSA at the microscopic level. As for the use of the instantaneous strain rate, it was utilized to realistically predict the deformation rate at each strain increment in our crystal plasticity approach [19]. The term  $d\tau_{CD}/dt$  denotes the time derivative of  $\tau_{CD}$ , i.e., Eq. (11), and by substitution of Eqs. (4) and (5) into the time derivative of Eq. (11), one obtains

$$\begin{aligned} \frac{d\tau_{CD}}{dt} = & -\frac{\mu}{2\pi(1-v)N_A} V_C \int_0^{2\pi} \int_{r_i}^{r_o} \frac{2C_0 [K(r, \alpha)D]^{\frac{2}{3}} \exp [-(K(r, \alpha)Dt_a)^{\frac{2}{3}}]}{3t_a^{\frac{1}{3}}} \\ & \left( 1 - \frac{t_a}{t_w} \right) \frac{\sin 2\alpha}{r} dr d\alpha \end{aligned} \quad (15)$$

**Table 1** The parameters and constants utilized in the current DSA model

$k$	$b$	$v$	$\mu$	$r_a$
$6.61 \times 10^{-5} \text{ eV K}^{-1}$	$2.58 \times 10^{-10} \text{ m}$	0.3	71 GPa	$126 \times 10^{-12} \text{ m}$
$V_c$	$r_c$	$v_D$	$E_0$	$S_{t0}$
$1.24 \times 10^{-6} \text{ m}^3 \text{ mol}^{-1}$	$70 \times 10^{-12} \text{ m}$	$1.38 \times 10^{13} \text{ s}^{-1}$	0.57 eV	1.04 GPa

Consequently, in its extended form, the modified Voce-hardening rule can be obtained from Eqs. (13)–(15) as in the following expression:

$$\begin{aligned} \tau^s = \tau_0 + (\tau_1 + \theta_1 \Gamma) \left( 1 - \exp \left( -\frac{\theta_0 \Gamma}{\tau_1} \right) \right) \\ - S M_i \frac{\mu}{2\pi(1-v)} \frac{V_c}{N_A} \int_0^{2\pi} \int_{r_i}^{r_0} \frac{2C_0 [K(r, \alpha)D]^{\frac{2}{3}} \exp \left[ (K(r, \alpha)Dt_a)^{\frac{2}{3}} \right]}{3t_a^{\frac{1}{3}}} \\ \left( 1 - \frac{t_a}{t_w} \right) \frac{\sin 2\alpha}{r} dr d\alpha \quad (16) \end{aligned}$$

It should be noted that, for the sake of brevity and to avoid repetition, only the key formulations of the fundamental VPSC algorithm are provided (Eqs. (12) and (13)). The readers are referred to Refs. [4,5,11,14,15,18,33], and [54–59] for the details of the original VPSC algorithm.

#### 4 Results and Discussion

The new hardening model detailed in Sec. 3 was incorporated into VPSC along with the experimentally measured initial textures of HS polycrystalline samples in order to predict the macroscopic deformation response of this material under uniaxial tensile loading with (Figs. 4–7) and without (Figs. 8–11) accounting for the

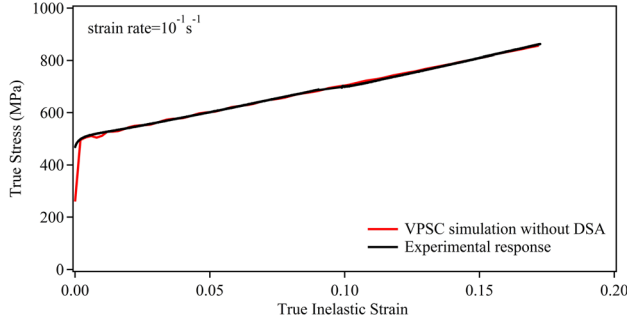


**Fig. 4** Comparison of experimental and VPSC simulation results of the uniaxial tensile deformation response of HS at a strain rate of  $1 \times 10^{-1} \text{ s}^{-1}$

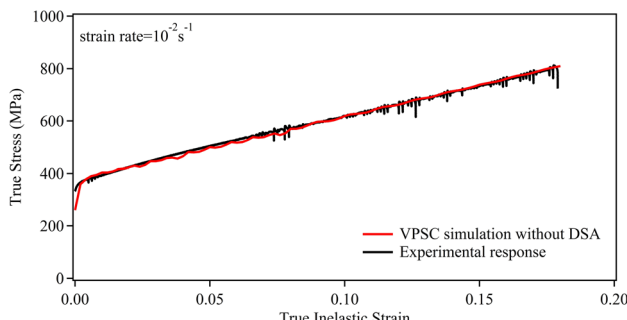


**Fig. 5** Comparison of experimental and VPSC simulation results of the uniaxial tensile deformation response of HS at a strain rate of  $1 \times 10^{-2} \text{ s}^{-1}$

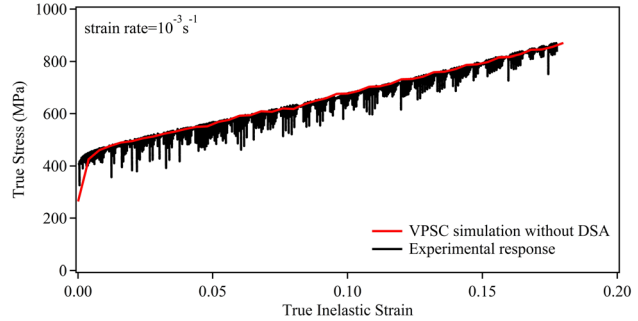


**Fig. 6** Comparison of experimental and VPSC simulation results of the uniaxial tensile deformation response of HS at a strain rate of  $1 \times 10^{-3} \text{ s}^{-1}$

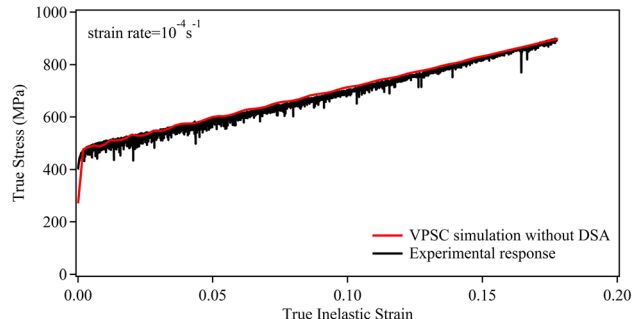


**Fig. 7** Comparison of experimental and VPSC simulation results of the uniaxial tensile deformation response of HS at a strain rate of  $1 \times 10^{-4} \text{ s}^{-1}$

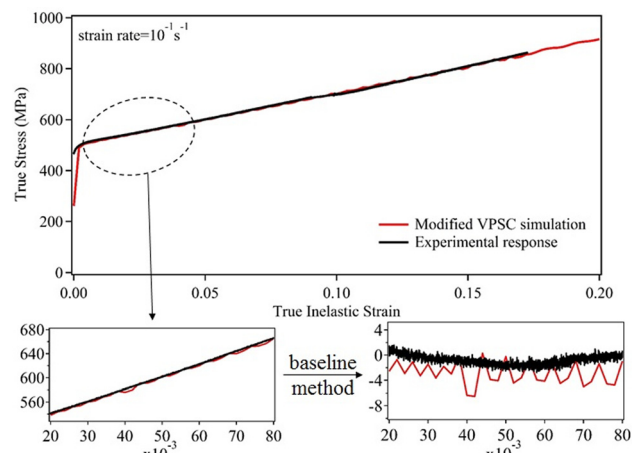


**Fig. 8** Comparison of experimental and modified VPSC simulation results of the uniaxial tensile deformation response of HS at a strain rate of  $1 \times 10^{-1} \text{ s}^{-1}$ . Both a specific stress-strain range and the corresponding baseline analysis result are provided in the insets. The horizontal and vertical axes of the graphs presented in the insets correspond to “true stress (MPa)” and “true inelastic strain,” respectively.

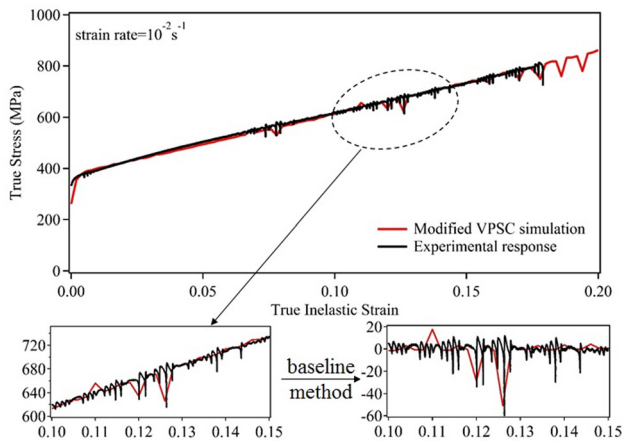


**Fig. 9** Comparison of experimental and modified VPSC simulation results of the uniaxial tensile deformation response of HS at a strain rate of  $1 \times 10^{-2} \text{ s}^{-1}$ . Both a specific stress-strain range and the corresponding baseline analysis result are provided in the insets. The horizontal and vertical axes of the graphs presented in the insets correspond to true stress (MPa) and true inelastic strain, respectively.

presence of DSA and NSRS. The true stress–true inelastic strain data were plotted in order to compare the initial and modified VPSC simulations and experimental response. One should also note that only the plastic deformation regime was modeled in the VPSC simulations since the VPSC only considers active plastic deformation up to necking, which is acceptable considering that the elastic deformation response of HS is not rate dependent [19].

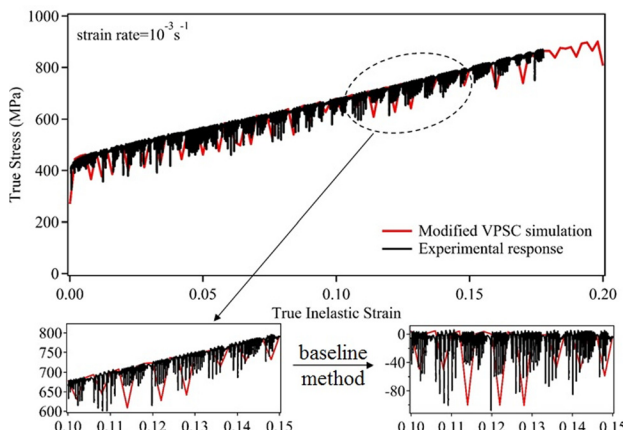


**Fig. 10** Comparison of experimental and modified VPSC simulation results of the uniaxial tensile deformation response of HS at a strain rate of  $1 \times 10^{-3} \text{ s}^{-1}$ . Both a specific stress-strain range and the corresponding baseline analysis result are provided in the insets. The horizontal and vertical axes of the graphs presented in the insets correspond to true stress (MPa) and true inelastic strain, respectively.

**Table 2** Voce-hardening parameters utilized in VPSC simulations for each strain rate

Strain rate ( $\text{s}^{-1}$ )	$\tau_0$ (MPa)	$\tau_0$ (MPa)	$\theta_0$ (MPa)	$\theta_1$ (MPa)
$1 \times 10^{-1}$	132	925	$53 \times 10^4$	350
$1 \times 10^{-2}$	132	147	$43 \times 10^3$	408
$1 \times 10^{-3}$	132	1580	$60 \times 10^4$	390
$1 \times 10^{-4}$	132	918	$55 \times 10^4$	398

It has been recently proven that the correct prediction of the macroscopic deformation response under any type of loading scenario can be achieved by the proper modeling of the microscale deformation based on the experimental data obtained from even the simplest case of the uniaxial tensile deformation [54,55]. Furthermore, the VPSC model has the strength of allowing for modifications of the hardening rule, which enables to account for the microstructural features and microdeformation mechanisms specific to each material. In particular, the deformation response of HS was previously modeled with VPSC to successfully account for the roles of several parameters on the strain hardening of this material, including slip–twin interactions, HDDWs, and precipitates [4,5,56]. Based on this previous experience, the DSA model proposed herein was incorporated into VPSC, which—to the best of our knowledge—constitutes the first example of incorporation of an atomic-level DSA model into crystal plasticity to predict the contributions of DSA and the resulting NSRS on the work-hardening response of HS. The novelty of the current approach is the computation of the shear stress contribution imposed on arrested dislocations leading to DSA at the atomic level, which is then implemented to the overall strain-hardening rule at the microscopic level utilizing VPSC.

For this purpose, the microscopic deformation response of HS was modeled at each strain rate using the experimental uniaxial deformation response at room temperature (Figs. 4–7). The standard VPSC model [58] was employed to predict the microscopic deformation response at each strain increment based on the classical Voce-hardening law. The reference strength of slip (i.e., the initial value of the critical resolved shear stress) was calculated as 132 MPa [18,59,60] and is provided in Table 2 along with the other Voce-hardening parameters that were obtained by fitting the simulated deformation response to the experimental one for each strain rate (Figs. 4–7). This reference strength value corresponds to the microscopic yield strength of the material, which relates to the macroscopic yield strength through Taylor factor computed based on the type of loading and initial texture of the material [18]. Even though different hardening parameters were used for each strain rate, the orders of magnitude of Voce-hardening parameters at different strain rates are either the same or very close to each other. In particular, these hardening parameters were determined by a step-by-step procedure based on a secant type of inclusion–matrix interaction, utilizing the experimentally determined initial texture, crystal structure, and number of grains of the material as input, and the experimental deformation response

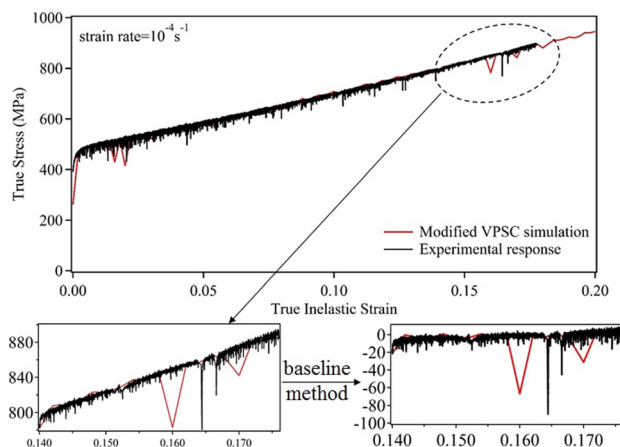


**Fig. 11** Comparison of experimental and modified VPSC simulation results of the uniaxial tensile deformation response of HS at a strain rate of  $1 \times 10^{-4} \text{ s}^{-1}$ . Both a specific stress-strain range and the corresponding baseline analysis result are provided in the insets. The horizontal and vertical axes of the graphs presented in the insets correspond to true stress (MPa) and true inelastic strain, respectively.

as a means of validation (Figs. 4–7). For all the simulations, large strain increments were used in order to assess the success of our modified crystal plasticity approach at large strain increments and also decrease the computational time. Consequently, these small fluctuations observed in the results of regular VPSC simulations stem from the purposely selected large strain increments. Material response accounting for DSA was modeled until moderate strain values, and the shape change of the grains was not considered during the simulations.

It should be noted that the second term of Eq. (14), which represents the contribution of DSA to the strain-hardening capacity, was ignored in the first set of standard VPSC simulations (Figs. 4–7). Accordingly, the results presented in Figs. 4–7 clearly demonstrate that the general work-hardening trend can be captured for all the four strain rates, however, the repeating stress striation patterns stemming from local instabilities in the stress-strain state facilitated by DSA and specific to each strain rate cannot be predicted.

The modified VPSC simulations, where the contribution of DSA was taken into account through the new hardening rule presented in Eq. (16), considered only the primary  $\{111\} <110>$  slip with 12 systems. The same Voce-hardening parameters were utilized as in the case of standard simulations in order to follow the same hardening trend and observe the contribution of the new atomic-scale model by adding an additional term to the classical Voce-hardening scheme to capture the solute atom effect on hardening. The scaling factor  $S$  of Eq. (14) was determined as 0.93 while predicting the experimental deformation response during modified VPSC simulations. The scaling factor reflects the contribution of the atomic-level DSA to the overall hardening response throughout the whole grain. It was originally considered as a fitting parameter to bridge the atomistic and microscopic scales; however, the value of the scaling factor turned out to be very close to 1, indicating that the model itself is quite precise even without a scaling/fitting factor. The corresponding modified VPSC simulation results are presented in Figs. 8–11 for the strain rates of  $10^{-4}$  to  $10^{-1}$   $s^{-1}$ , along with the corresponding baseline analyses (insets of Figs. 8–11). Specifically, a baseline method was utilized in order to better visualize the corresponding improvement on the prediction of the stress-strain behavior by the modified VPSC simulation: a line equation fitting two points, namely, the onset and the end of plastic region, was derived, and then, the true stress values from the experimental and numerical strain values were recalculated utilizing this equation. Finally, the difference between the recalculated and initial values of true stress was plotted. The corresponding results demonstrate the accuracy and precision of the proposed model more clearly, including the serrations in the deformation response of HS stemming from the DSA. The predicted deformation curves not only follow the correct hardening trend for each strain rate but also reflect the effect of DSA on the strain hardening, which is evident from the close prediction of the repeating stress striation patterns specific to each strain rate utilizing the same model.

It is important to note that an increase in the strain rate causes a decline in the waiting time as the Orowan equation suggests, which implies that the C atoms pin the dislocations for a lesser time period. However, increase in strain rate provides additional energy to the system, which should be dissipated by the dislocation movements, C atom diffusivity, or other microstructural interactions. Analytically, the waiting time has significant effect on the time derivative of  $\tau_{CD}$ , as Eq. (15) suggests. Nevertheless, this term also depends on aging time, which is also a function of the waiting time. Therefore, based on the analytical and conceptual descriptions, it cannot be concluded that C effects on the deformation response of HS vary at each strain increment, which causes plastic instabilities during the material flow that are more pronounced at low strain rates [14,19]. The current model successfully predicts such plastic instabilities both at the low and moderate inelastic strain values (Figs. 8–11), such that the instantaneous changes in the material response can be well represented.

Overall, the new crystal plasticity modeling approach not only predicts the relatively more stable deformation response at high strain rates (e.g.,  $10^{-1}$   $s^{-1}$ , Fig. 8), but also provides a very good estimate of the unstable plastic deformation response exhibiting larger stress striations at lower strain rates (Figs. 10 and 11). Moreover, the current model successfully captures the NSRS exhibited by HS, which ensures that the current approach can be adopted to predict the deformation response of rate-sensitive metallic materials.

## 5 Conclusions

A new crystal plasticity modeling approach was proposed to predict the roles of DSA and the resulting NSRS on the unusually high work-hardening capacity of HS. For this purpose, the room temperature macroscopic deformation response of HS polycrystals was examined with the aid of monotonic and strain jump experiments under uniaxial tensile loading within the  $10^{-4}$  to  $10^{-1}$   $s^{-1}$  strain rate range. Specifically, a unique strain-hardening model was proposed that incorporates the atomic-level local instabilities due to the pinning of dislocations by diffusing carbon atoms to the classical Voce hardening. The simulation results demonstrated that the new modeling approach presented herein not only successfully predicts the role of DSA and the resulting NSRS on the macroscopic deformation response of HS but also opens a new venue for accurately predicting the deformation response of rate-sensitive metallic materials.

## Acknowledgment

This study was funded by the Scientific and Technological Research Council of Turkey (TÜBİTAK) under Grant No. 112M806 and partially by the Koç University TÜPRAŞ Energy Center (KÜTEM) Seed Funding Program.

## References

- [1] Dastur, Y. N., and Leslie, W. C., 1981, "Mechanism of Work Hardening in Hadfield Manganese Steel," *Metall. Trans. A*, **12**(5), pp. 749–759.
- [2] Adler, P. H., Olson, G. B., and Owen, W. S., 1986, "Strain Hardening of Hadfield Manganese Steel," *Metall. Trans. A*, **17**(10), pp. 1725–1737.
- [3] Efstathiou, C., and Sehitoglu, H., 2010, "Strain Hardening and Heterogeneous Deformation During Twinning in Hadfield Steel," *Acta Mater.*, **58**(5), pp. 1479–1488.
- [4] Karaman, I., Sehitoglu, H., Gall, K., Chumlyakov, Y. I., and Maier, H. J., 2000, "Deformation of Single Crystal Hadfield Steel by Twinning and Slip," *Acta Mater.*, **48**(6), pp. 1345–1359.
- [5] Canadinc, D., Sehitoglu, H., Maier, H. J., and Chumlyakov, Y. I., 2005, "Strain Hardening Behavior of Aluminum Alloyed Hadfield Steel Single Crystals," *Acta Mater.*, **53**(6), pp. 1831–1842.
- [6] Feng, X. Y., Zhang, F. C., Yang, Z. N., and Zhang, M., 2013, "Wear Behaviour of Nanocrystallised Hadfield Steel," *Wear*, **305**(1–2), pp. 299–304.
- [7] Atabaki, M. M., Jafari, S., and Abdollah-Pour, H., 2012, "Abrasive Wear Behavior of High Chromium Cast Iron and Hadfield Steel—A Comparison," *J. Iron Steel Res. Int.*, **19**(4), pp. 43–50.
- [8] Kang, J., Zhang, F. C., Long, X. Y., and Lv, B., 2014, "Cyclic Deformation and Fatigue Behaviors of Hadfield Manganese Steel," *Mater. Sci. Eng. A*, **591**, pp. 59–68.
- [9] Petrov, Y. N., Gavriljuk, V. G., Berns, H., and Schmalt, F., 2006, "Surface Structure of Stainless and Hadfield Steel After Impact Wear," *Wear*, **260**(6), pp. 687–691.
- [10] Efstathiou, C., and Sehitoglu, H., 2009, "Strengthening Hadfield Steel Welds by Nitrogen Alloying," *Mater. Sci. Eng. A*, **506**(1–2), pp. 174–179.
- [11] Canadinc, D., 2005, "A Detailed Investigation of the Strain Hardening Response of Aluminum Alloyed Hadfield Steel," Ph.D. thesis, University of Illinois at Urbana-Champaign, Champaign, IL.
- [12] Owen, W. S., and Gruijicic, M., 1999, "Strain Aging of Austenitic Hadfield Manganese Steel," *Acta Mater.*, **47**(1), pp. 111–126.
- [13] Raghavan, K. S., Sastri, A. S., and Marcinkowski, M. J., 1969, "Nature of the Work-Hardening Behavior in Hadfield's Manganese Steel," *Trans Metall. Soc. AIME*, **245**, pp. 1569–1575.
- [14] Karaman, I., Sehitoglu, H., Beaudoin, A. J., Chumlyakov, Y. I., Maier, H. J., and Tome, C. N., 2000, "Modeling the Deformation Behavior of Hadfield Steel Single and Polycrystals Due to Twinning and Slip," *Acta Mater.*, **48**(9), pp. 2031–2047.
- [15] Karaman, I., Sehitoglu, H., Chumlyakov, Y. I., Maier, H. J., and Kireeva, I. V., 2001, "The Effect of Twinning and Slip on the Bauschinger Effect of Hadfield Steel Single Crystals," *Metall. Mater. Trans. A*, **32**(13), pp. 695–706.

- [16] Karaman, I., Sehitoglu, H., Chumlyakov, Y., Maier, H., and Kireeva, I., 2001, "Extrinsic Stacking Faults and Twinning in Hadfield Manganese Steel Single Crystals," *Scr. Mater.*, **44**(2), pp. 337–343.
- [17] Shtremel, M. A., and Kovalenko, I. A., 1987, "On the Work Hardening Mechanism of Hadfield Steel," *Phys. Met. Metall.*, **63**, pp. 158–166.
- [18] Canadine, D., Sehitoglu, H., and Maier, H. J., 2007, "The Role of Dense Dislocation Walls on the Deformation Response of Aluminum Alloyed Hadfield Steel Polycrystals," *Mater. Sci. Eng. A*, **454–455**, pp. 662–666.
- [19] Canadine, D., Efsthathiou, C., and Sehitoglu, H., 2008, "On the Negative Strain Rate Sensitivity of Hadfield Steel," *Scr. Mater.*, **59**(10), pp. 1103–1106.
- [20] Cottrell, A. H., and Bilby, B. A., 1948, "Dislocation Theory of Yielding and Strain Ageing of Iron," *Proc. Phys. Soc. Lond. A*, **49**(62), pp. 49–62.
- [21] Cottrell, A. H., and Jaswon, M. A., 1949, "Distribution of Solute Atoms Round a Slow Dislocation," *Proc. R. Soc. A*, **199**(1056), pp. 104–114.
- [22] Huang, Z. Y., Chaboche, J.-L., Wang, Q. Y., Wagner, D., and Bathias, C., 2014, "Effect of Dynamic Strain Aging on Isotropic Hardening in Low Cycle Fatigue for Carbon Manganese Steel," *Mater. Sci. Eng. A*, **589**, pp. 34–40.
- [23] van Den Brink, S. H., Van Den Beukel, A., and McCormick, P. G., 1975, "Strain Rate Sensitivity and the Portevin-Le Chatelier Effect in Au–Cu Alloys," *Phys. Status Solidi*, **30**(2), pp. 469–477.
- [24] Louat, N., 1981, "On the Theory of the Portevin-Le Chatelier Effect," *Scr. Metall.*, **15**(11), pp. 1167–1170.
- [25] McCormick, P. G., 1988, "Theory of Flow Localisation Due to Dynamic Strain Ageing," *Acta Metall.*, **36**(12), pp. 3061–3067.
- [26] Estrin, Y., and McCormick, P. G., 1991, "Modelling the Transient Flow Behaviour of Dynamic Strain Ageing Materials," *Acta Metall. Mater.*, **39**(12), pp. 2977–2983.
- [27] McCormick, P. G., and Ling, C. P., 1995, "Numerical Modelling of the Portevin-Le Chatelier Effect," *Acta Metall. Mater.*, **43**(5), pp. 1969–1977.
- [28] Wang, C., Li, Z., Xu, Y., and Han, E., 2007, "Acoustic Emission Inspection of Portevin-Le Chatelier Effect and Deformation Mechanisms of Two Mg–Li–Al Alloys," *J. Mater. Sci.*, **42**(10), pp. 3573–3579.
- [29] Renard, K., Ryelandt, S., and Jacques, P. J., 2010, "Characterisation of the Portevin-Le Chatelier Effect Affecting an Austenitic TWIP Steel Based on Digital Image Correlation," *Mater. Sci. Eng. A*, **527**(12), pp. 2969–2977.
- [30] Chmelík, F., Klose, F. B., Dierke, H., Sachl, J., Neuhäuser, H., and Lukáč, P., 2007, "Investigating the Portevin-Le Chatelier Effect in Strain Rate and Stress Rate Controlled Tests by the Acoustic Emission and Laser Extensometry Techniques," *Mater. Sci. Eng. A*, **462**(1–2), pp. 53–60.
- [31] Yilmaz, A., 2011, "The Portevin-Le Chatelier Effect: A Review of Experimental Findings," *Sci. Technol. Adv. Mater.*, **12**(6), p. 063001.
- [32] van den Beukel, A., 1975, "Theory of the Effect of Dynamic Strain Aging on Mechanical Properties," *Phys. Status Solidi*, **30**(1), pp. 197–206.
- [33] Canadine, D., 2001, "The Effect of Nitrogen and Aluminum on the Deformation Behavior of Hadfield Manganese Steel Single Crystals," M.S. thesis, University of Illinois at Urbana-Champaign, Champaign, IL.
- [34] Kubin, L. P., Estrin, Y., and Perrier, C., 1992, "On Static Strain Ageing," *Acta Metall. Mater.*, **40**(5), pp. 1037–1044.
- [35] Ling, C. P., and McCormick, P. G., 1990, "Strain Rate Sensitivity and Transient Behaviour in an Al Mg Si Alloy," *Acta Metall. Mater.*, **38**(12), pp. 2631–2635.
- [36] Soare, M. A., and Curtin, W. A., 2008, "Single-Mechanism Rate Theory for Dynamic Strain Aging in fcc Metals," *Acta Mater.*, **56**(15), pp. 4091–4101.
- [37] Soare, M. A., and Curtin, W. A., 2008, "Solute Strengthening of Both Mobile and Forest Dislocations: The Origin of Dynamic Strain Aging in fcc Metals," *Acta Mater.*, **56**(15), pp. 4046–4061.
- [38] Anjabin, N., Taheri, A. K., and Kim, H. S., 2013, "Simulation and Experimental Analyses of Dynamic Strain Aging of a Supersaturated Age Hardenable Aluminum Alloy," *Mater. Sci. Eng. A*, **585**, pp. 165–173.
- [39] Narayanan, S., McDowell, D. L., and Zhu, T., 2014, "Crystal Plasticity Model for BCC Iron Atomistically Informed by Kinetics of Correlated Kinkpair Nucleation on Screw Dislocation," *J. Mech. Phys. Solids*, **65**, pp. 54–68.
- [40] Friedel, J., 1964, *Dislocations*, Pergamon Press, Oxford, UK.
- [41] Kang, K., Yin, J., and Cai, W., 2014, "Journal of the Mechanics and Physics of Solids Stress Dependence of Cross Slip Energy Barrier for Face-Centered Cubic Nickel," *J. Mech. Phys. Solids*, **62**, pp. 181–193.
- [42] Springer, F., Nortmann, A., and Schwink, C., 1998, "A Study of Basic Processes Characterizing Dynamic Strain Ageing," *Phys. Status Solidi A*, **170**(1), pp. 63–81.
- [43] Ono, K., 1968, "Temperature Dependence of Dispersed Barrier Hardening," *J. Appl. Phys.*, **39**(3), pp. 1803–1806.
- [44] Peter, H., 1996, "On the Physics of the Portevin-Le Chatelier Effect—Part 1: The Statistics of Dynamic Strain Ageing," *Mater. Sci. Eng. A*, **207**(2), pp. 208–215.
- [45] Bayley, C. J., Brekelmans, W. A. M., and Geers, M. G. D., 2006, "A Comparison of Dislocation Induced Back Stress Formulations in Strain Gradient Crystal Plasticity," *Int. J. Solids Struct.*, **43**(24), pp. 7268–7286.
- [46] Vallée, C., Fortuné, D., and Lerintiu, C., 2008, "On the Dual Variable of the Cauchy Stress Tensor in Isotropic Finite Hyperelasticity," *C. R. Mécanique*, **336**(11–12), pp. 851–855.
- [47] Bell, J. F., 1995, "Laboratory Experiments on Thin-Walled Tubes at Large Finite Strain: Symmetry, Coaxiality, Rigid Body Rotation, and the Role of Invariants, for the Applied Stress  $\sigma = RT_R^{-T}$ , the Cauchy Stress  $\sigma^* = [III_V]^{-1}F_R^{-T}$ , and the Left Cauchy-Green Stretch Tensor," *Int. J. Plast.*, **11**(1), pp. 119–144.
- [48] Kalidindi, S. R., Bronkhorst, C. A., and Anand, L., 1992, "Crystallographic Texture Evolution in Bulk Deformation Processing of FCC Metals," *J. Mech. Phys. Solids*, **40**(3), pp. 537–569.
- [49] Patra, A., Zhu, T., and McDowell, D. L., 2014, "Constitutive Equations for Modeling Non-Schmid Effects in Single Crystal bcc-Fe at Low and Ambient Temperatures," *Int. J. Plast.*, **59**, pp. 1–14.
- [50] Jörn, H., 1999, "A Crystallographic Model for the Study of Local Deformation Processes in Polycrystals," *Int. J. Plast.*, **15**(6), pp. 605–624.
- [51] Evers, L. P., Brekelmans, W. A. M., and Geers, M. G. D., 2004, "Scale Dependent Crystal Plasticity Framework With Dislocation Density and Grain Boundary Effects," *Int. J. Solids Struct.*, **41**(18–19), pp. 5209–5230.
- [52] Sofronis, P., and Birnbaum, H. K., 1995, "Mechanics of the Hydrogen-Dislocation-Impurity Interactions—Part I: Increasing Shear Modulus," *J. Mech. Phys. Solids*, **43**(1), pp. 49–90.
- [53] Voce, E., 1948, "The Relationship Between Stress and Strain for Homogeneous Deformation," *J. Inst. Met.*, **74**, pp. 537–562.
- [54] Canadine, D., Ryelandt, S., and Jacques, P. J., 2010, "Experimental and Numerical Investigation of the Role of Grain Boundary Misorientation Angle on the Dislocation–Grain Boundary Interactions," *Adv. Eng. Mater.*, **13**(4), pp. 281–287.
- [55] Onal, O., Ozmeni, C., and Canadine, D., 2014, "Multi-Scale Modeling of the Impact Response of a Strain-Rate Sensitive High-Manganese Austenitic Steel," *Front. Mater.*, **1**, p. 16.
- [56] Canadine, D., Karaman, I., Sehitoglu, H., Chumlyakov, Y. I., and Maier, H. J., 2003, "The Role of Nitrogen on the Deformation Response of Hadfield Steel Single Crystals," *Metall. Mater. Trans. A*, **34**(9), pp. 1821–1831.
- [57] Onal, O., Bal, B., Toker, S. M., Mirzajanzadeh, M., Canadine, D., and Maier, H. J., 2014, "Microstructure-Based Modeling of the Impact Response of a Biomedical Niobium–Zirconium Alloy," *J. Mater. Res.*, **29**(10), pp. 1123–1134.
- [58] Leibsohn, R. A., and Tomé, C. N., 1993, "A Self-Consistent Anisotropic Approach for the Simulation of Plastic Deformation and Texture Development of Polycrystals: Application to Zirconium Alloys," *Acta Metall. Mater.*, **41**(9), p. 2611.
- [59] Canadine, D., Sehitoglu, H., Maier, H. J., and Kurath, P., 2008, "On the Incorporation of Length Scales Associated With Pearlitic and Bainitic Microstructures Into a Visco-Plastic Self-Consistent Model," *Mater. Sci. Eng. A*, **485**(1–2), p. 258.
- [60] Bishop, J. F. W., and Hill, R., 1951, "XLVI. A Theory of the Plastic Distortion of a Polycrystalline Aggregate Under Combined Stresses," *Phil. Mag.*, **42**(327), pp. 414–427.